Supplementary material for "Deep Generalization of Structured Low-Rank Algorithms (Deep-SLR)"

Aniket Pramanik, Hemant Aggarwal, Mathews Jacob
The University of Iowa, USA

***Abstract*—We show results from additional experiments on single-channel and parallel MRI recovery. Later we discuss the application of our proposed schemes for diffusion MRI recovery and compare those with the state-of-the-art methods.**

I. Single-channel Signal Recovery

The proposed approaches for single-channel recovery are compared against the state-of-the-art in Table S1. The methods were tested on single-channel knee (coronal and sagittal view), and brain data mentioned in Section IV-A in the main paper. The mean SNR, PSNR and SSIM values with corresponding standard deviations were calculated for 2560 (10 subjects) brain, and 420 (3 subjects) knee (sagittal and coronal) slices, respectively. The coronal knee and brain were 4x under-sampled while the sagittal knee was 6x under-sampled. The proposed k-space network K-DSLR outperforms K-UNET (k-space UNET) and I-UNET (image-space UNET). K-DSLR performance is comparable to calibration-less approach GIRAF that motivates the proposed scheme. The addition of spatial domain prior in H-DSLR improves performance significantly over GIRAF.

We compare reconstruction quality of single-channel coronal and sagittal knee slices in Fig. S2 and Fig. S3, respectively. The K-DSLR and H-DSLR reconstructions are that of a $K = 10$ iteration model. We observe that K-DSLR results are comparable to model-based GIRAF. By contrast, our proposed model-based schemes outperform direct inversion approaches, K-UNET, and I-UNET. Note that our proposed schemes have much smaller number of trainable parameters compared to the UNETs. The multiple iterations of the proposed alternating strategy improves overall performance. An addition of spatial domain prior in H-DSLR visibly improves reconstruction quality, and SNR. The yellow arrows in the zoomed cartilage region point out differences in the preservation of minute structures. K-UNET and I-UNET seem to be missing lot of details as pointed out by the arrows. Although GIRAF and K-DSLR reconstructions miss few details, the H-DSLR scheme preserves all of those. The H-DSLR reconstructions are better in terms of SNR than other methods considered here.

Aniket Pramanik, Hemant Aggarwal and Mathews Jacob are from the Department of Electrical and Computer Engineering at the University of Iowa, Iowa City, IA, 52242, USA (e-mail: aniket-pramanik@uiowa.edu; hemantkumar-aggarwal@uiowa.edu; mathews-jacob@uiowa.edu). This work is supported by grant NIH 1R01EB019961-01A1.

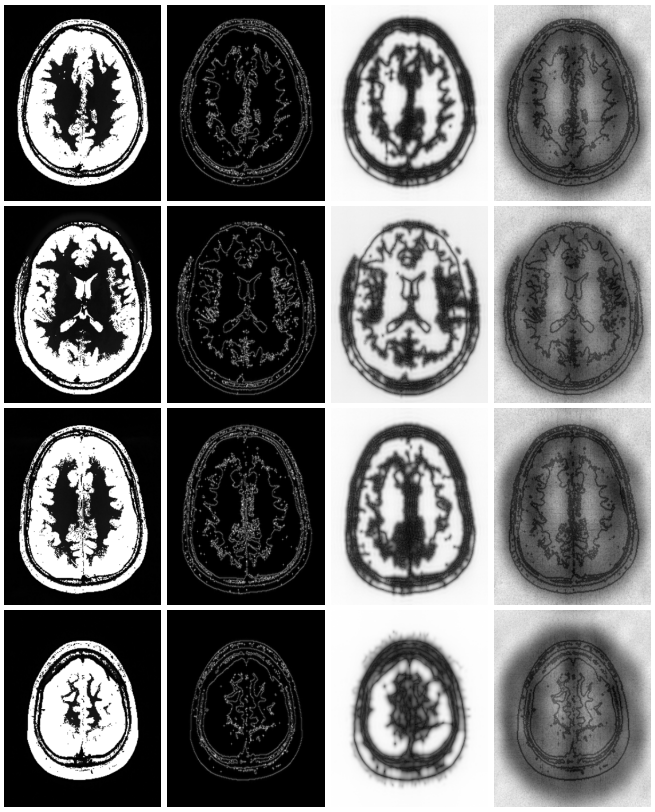

(a) Piecewise constant (b) Gradient (c) SOS-$\mathcal{R}$ (d) SOS-$\mathcal{N}_{\mathrm{k}}$

Fig. S1. Illustration of linear and non-linear annihilation operators on piecewise constant images. The images and their gradients are shown in (a) and (b) respectively. The SOS-$\mathcal{R}$ is the sum of squares function on linear annihilation operator $\mathcal{R}$ from SLR schemes that kills edges or high gradient regions as shown in (c). The non-linear extension of SOS-$\mathcal{R}$ is SOS-$\mathcal{N}_{\mathrm{k}}$ and its outputs are shown in (d) which closely match to (c). The non-linear operation is generalizable across variety of brain slices shown here.

We show results of hypothesis test (described in Section V-B in the main paper) on single-channel brain slices with different anatomies in Fig. S1. The proposed k-space network learns non-linear annihilation relations that can kill edges or high gradient regions in piecewise constant images. The results in Fig. S1 show that the non-linear block $\mathcal{N}_{\mathrm{k}}$ can linearly approximate the annihilation relations which closely match with those learnt by the SLR schemes. Specifically, the SOS-$\mathcal{N}_{\mathrm{k}}$ outputs of the perturbations for each case in Fig. S1.(d) are

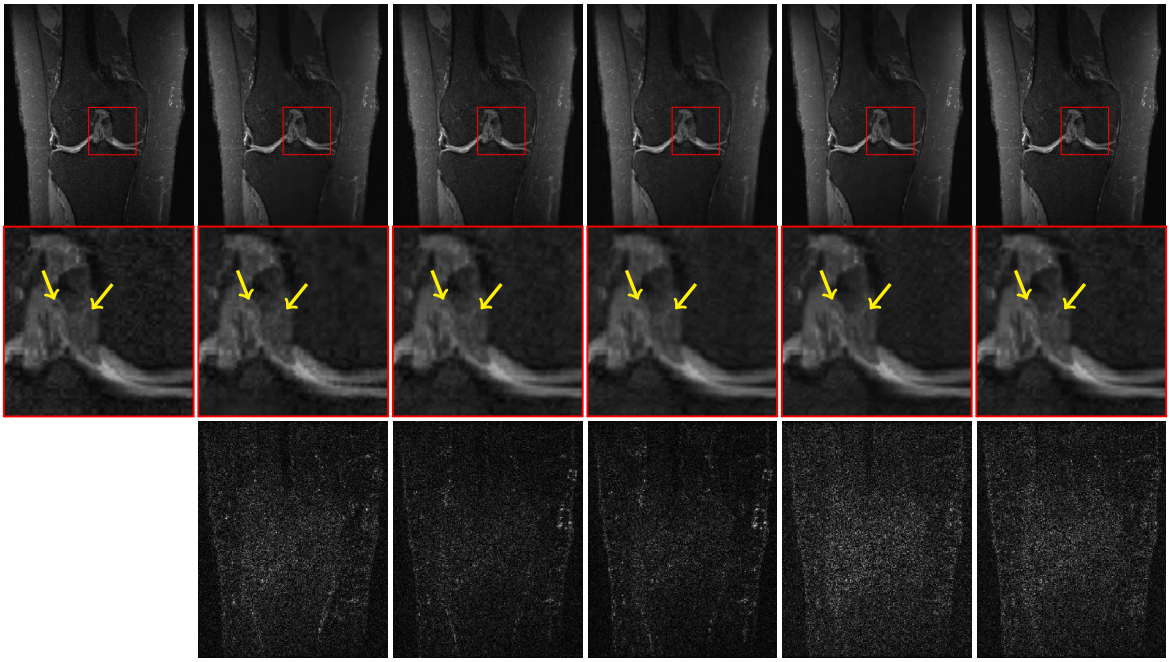

(a) Fully sampled | (b) GIRAF 18.26 / 25.14 / 0.841 | (c) K-UNET 17.65 / 24.57 / 0.828 | (d) **K-DSLR** **18.75 / 25.81 / 0.853** | (e) I-UNET 17.33 / 24.19 / 0.831 | (f) **H-DSLR** **19.37 / 26.59 / 0.859**

Fig. S2. Reconstruction results of 6-fold accelerated single-channel knee data with coronal view. SNR (dB)/ PSNR (dB)/ SSIM values are reported for each case. The top row displays reconstructions (magnitude images) while the bottom row displays corresponding error maps. The yellow arrows point out the differences in the zoomed coronal view of cartilage region. The proposed schemes outperform state-of-the-art schemes and preserve complex structures better as pointed out by arrows.

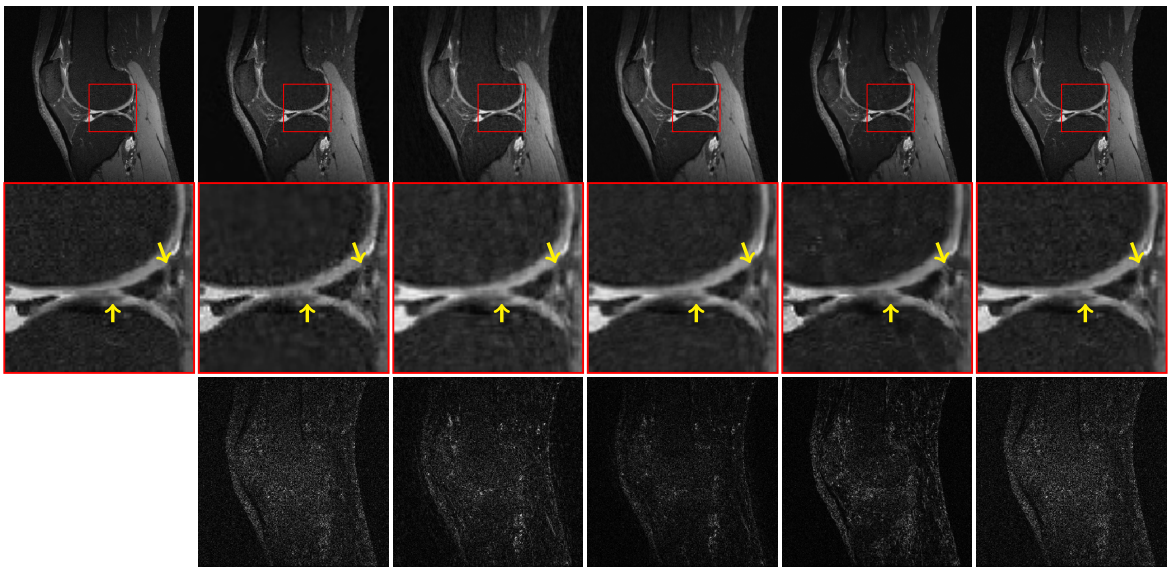

(a) Fully sampled | (b) GIRAF 19.02/ 28.09 / 0.880 | (c) K-UNET 18.81 / 27.74 / 0.875 | (d) **K-DSLR** **19.33 / 28.41 / 0.884** | (e) I-UNET 18.51 / 27.39 / 0.871 | (f) **H-DSLR** **22.58 / 31.63 / 0.924**

Fig. S3. Reconstruction results of 4-fold accelerated single-channel knee data with sagittal view. SNR (dB)/ PSNR (dB)/ SSIM values are reported for each case. The top row displays reconstructions (magnitude images) while the bottom row displays corresponding error maps. The yellow arrows point out the differences in the zoomed sagittal view of cartilage region. The proposed schemes recover finer details better compared to others.

similar to SOS-$\mathcal{R}$ outputs in Fig. S1.(c) from SLR schemes. Thus, the non-linear annihilation block $\mathcal{N}_{\text{k}}$ is generalizable over a variety of brain anatomy slices.

II. Parallel MRI Recovery

We study robustness of the proposed H-DSLR scheme to acceleration factors for variety of slices from the test subjects. In Fig. S4, we show reconstructions of multi-channel brain dataset for 4x, 6x and 10x accelerations over several anatomies

Signal-to-Noise Ratio (SNR)			
Organ	Knee Coronal	Knee Sagittal	Brain (CCP)
Acceleration	6x	4x	4x
Methods	SNR	SNR	SNR
GIRAF	18.14 ± 1.58	19.01 ± 1.64	22.02 ± 1.36
K-UNET	17.76 ± 1.29	18.78 ± 1.54	19.78 ± 1.47
K-DSLR	18.69 ± 1.08	19.16 ± 1.11	21.18 ± 1.01
I-UNET	17.29 ± 1.77	18.53 ± 1.83	19.43 ± 1.59
H-DSLR	19.31 ± 1.02	22.48 ± 1.26	25.39 ± 0.84
Peak Signal-to-Noise Ratio (PSNR)			
Organ	Knee Coronal	Knee Sagittal	Brain (CCP)
Acceleration	6x	4x	4x
Methods	SNR	SNR	SNR
GIRAF	25.01 ± 1.55	27.96 ± 1.59	29.11 ± 1.41
K-UNET	24.55 ± 1.34	27.75 ± 1.52	26.68 ± 1.43
K-DSLR	25.64 ± 1.02	28.22 ± 1.03	28.27 ± 0.97
I-UNET	24.34 ± 1.79	27.49 ± 1.87	26.47 ± 1.63
H-DSLR	26.46 ± 0.98	31.54 ± 1.18	32.53 ± 0.87
Structural Similarity (SSIM)			
Organ	Knee Coronal	Knee Sagittal	Brain (CCP)
Acceleration	6x	4x	4x
Methods	SSIM	SSIM	SSIM
GIRAF	0.841 ± 0.031	0.877 ± 0.040	0.915 ± 0.023
K-UNET	0.830 ± 0.029	0.872 ± 0.032	0.842 ± 0.019
K-DSLR	0.849 ± 0.019	0.878 ± 0.025	0.902 ± 0.017
I-UNET	0.834 ± 0.028	0.873 ± 0.026	0.838 ± 0.026
H-DSLR	0.852 ± 0.011	0.921 ± 0.013	0.929 ± 0.009

TABLE S1
QUANTITATIVE COMPARISON OF SLR, DEEP-SLR AND UNET RECONSTRUCTIONS IN THE CONTEXT OF SINGLE-CHANNEL RECOVERY. THE BOLD-FACED METHODS ARE THE PROPOSED ONES.

of a test subject. We train a $K = 10$ iteration H-DSLR network end-to-end with 10x under-sampled brain slices and test it on 4x, 6x, 10x slices from subjects unseen by the network. The dataset is the one mentioned in Section IV-A from the main paper. These reconstructions are appreciable over a range of slices including the corner ones. The brain structure is preserved in all the cases; 4x and 6x reconstructions have sharper edges compared to 10x. The minute structures in the cerebellum region are better preserved in 4x compared to the other two which is due to lower acceleration. The 10x reconstruction loses few details in the cerebellum region but preserves most of the gray and white matter; 6x preserves all of them but appears slightly blurred compared to 4x. The proposed scheme could generalize appreciably over a variety of unseen brain slices at different acceleration factors.

We perform a similar study for multi-channel knee dataset described in Section IV-A in the main paper. In Fig. S5, we display 3x and 4x reconstructions from different anatomies of a test subject. Similar to brain, we train a $K = 10$ iteration H-DSLR network with 4x under-sampled knee slices and test it on 3x, 4x slices from unseen subjects. The reconstructions appear significantly de-aliased for all cases. The cartilage region has several minute details which are slightly better preserved for the 3x case. Overall, the proposed scheme could de-alias variety of slices including the corner ones for different acceleration factors which shows its generalizability.

The plot in Fig. S6 shows the effect of increasing iterations K of our proposed scheme for parallel MRI cases. We observe a similar trend for 6x under-sampled brain and 4x under-sampled knee respectively. The average SNR on test data improves as we increase the iterations. Thus, unrolling the optimization blocks for several iterations is beneficial. Since, the performance saturated after 10^{th} iteration, we chose $K = 10$ for parallel MRI experiments. We also observed $K = 10$ iteration model to be optimal for single-channel experiments.

We show the intermediate results of H-DSLR algorithm as a function of iterations in Fig. S7. We note that for both

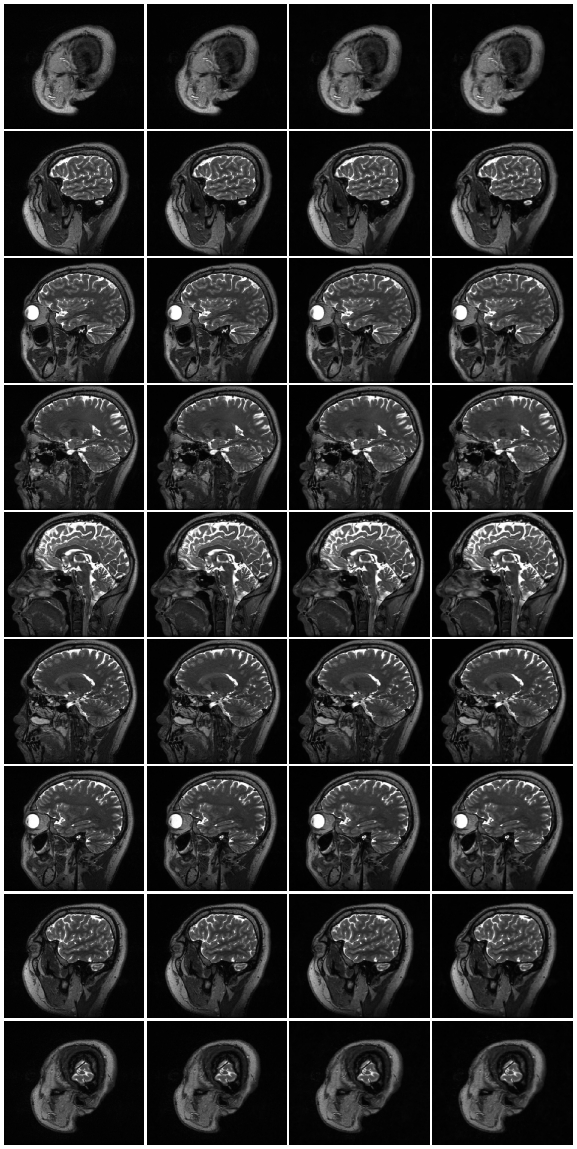

(a) Fully sampled (b) 4x recon (c) 6x recon (d) 10x recon

Fig. S4. Proposed H-DSLR reconstructions of 12-channel brain data for 4x, 6x and 10x accelerations. The displayed images are sum-of-squares reconstructions. H-DSLR is robust to acceleration factors for different anatomies of brain.

knee and brain test data, aliasing reduces as a function of iterations upto $K = 10$. The reduction in aliasing with more iterations justifies the benefit of unrolling the proposed scheme for more iterations. The amount of reduction in aliasing with iterations is more initially and saturates afterwards around 9-10 iterations. Thus, visible aliasing is reduced with increase in iterations which provides improved SNR.

III. DIFFUSION MRI RECOVERY

A. Structured Low Rank Algorithms for Multi-shot Echo Planar Imaging (EPI) Acquisition

Multi-shot annihilation relations exist for phase-corrupted images as shown in [1], in addition to the multi-channel annihilation relations discussed before. The phase-corrupted

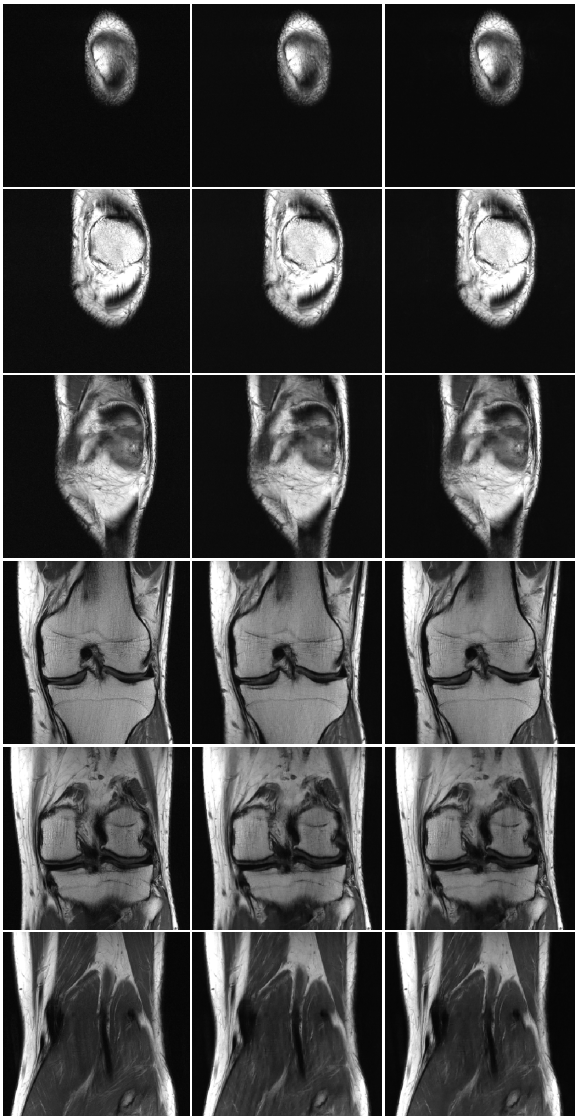

(a) Fully sampled (b) 3x recon (c) 4x recon

Fig. S5. Proposed H-DSLR reconstructions of 15-channel knee data for 3x and 4x accelerations. The displayed images are sum-of-squares reconstructions. H-DSLR is robust to acceleration factors for different anatomies of knee.

images $\boldsymbol{\gamma}_i[\mathbf{r}]$, $i = 1 \dots N$ satisfy a pairwise Fourier domain annihilation relation $\widehat{\boldsymbol{\gamma}_i}[\mathbf{k}] * \widehat{\boldsymbol{\phi}_j}[\mathbf{k}] - \widehat{\boldsymbol{\gamma}_j}[\mathbf{k}] * \widehat{\boldsymbol{\phi}_i}[\mathbf{k}] = 0, \forall \mathbf{k}$, where $\widehat{\boldsymbol{\gamma}_i}[\mathbf{k}]$ and $\widehat{\boldsymbol{\phi}_i}[\mathbf{k}]$ are the Fourier coefficients of $\boldsymbol{\gamma}_i(\mathbf{k})$ and $\boldsymbol{\phi}_i(\mathbf{k})$ respectively. The $\boldsymbol{\phi}_i[\mathbf{r}]$ are smooth phase images. The relations for each pair of phase-corrupted images can be compactly written as in (5). Similar to the parallel imaging case, the Hankel matrices corresponding to each shot and channel are stacked horizontally to obtain $\mathcal{T}(\widehat{\boldsymbol{\Gamma}})$, which is low rank due to large null space $\mathbf{N}$. The columns of $\mathbf{N}$ are vertically stacked filters $\widehat{\boldsymbol{\phi}_i}$. In this case, $\mathcal{G} = \mathcal{I}$ (identity mapping). This lifting is similar to the parallel imaging case but with different annihilation relations.

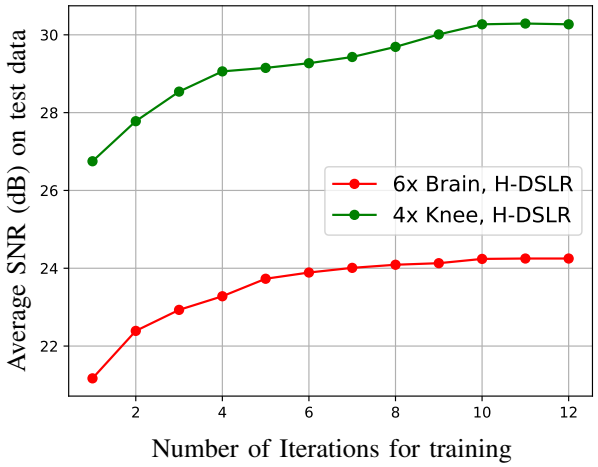

Fig. S6. Performance improvement in terms of average SNR (dB) on 6x accelerated 12-channel brain and 4x accelerated 15-channel knee test data respectively. The average testing SNR improves till $K = 10$ iteration and saturates afterwards.

B. CNN Architecture for Diffusion MRI Recovery

For this application we use the MIMO version of modified 12-layer UNET as $\mathcal{N}_{\mathrm{k}}$. The number of input and output channels are set according to complex channels in the dataset which is calculated as $N = N_{sh} \times N_{coil}$ where N_{sh} denotes number of shots per acquisition while N_{coil} corresponds to the number of coils used. Similar to other applications, we ensure the number of trainable parameters are same for both K-DSLR and H-DSLR. The regularization parameters were fixed at $\lambda = 1$, $\beta = 1$. We chose $K = 3$ iteration model based on performance which saturated with further iterations. All other training parameters were kept similar to other experiments.

C. Data Acquisition

For diffusion MRI experiments, four-shot EPI data of seven healthy subjects were obtained from [2]. The subjects were scanned in a 3T scanner using 32-channel head coil. The number of gradient directions were 60 per slice with the parameters: FOV = 210 x 210 mm, TE = 84 ms, slice thickness = 4 mm and a matrix size of 256 x 152 with partial Fourier oversampling of 24 lines. The dataset was split into 68 training slices from five subjects, five validation slices from the sixth subject and six testing slices from the seventh subject. Each slice had 60 directions. Similar to [2], the IRLS-MUSSELS (IRLS-M) [3] reconstructions were used as ground truth for training and quantitative comparisons.

D. State-of-the-art Methods for Comparison

For diffusion MRI experiments, we compare our proposed scheme with MoDL-MUSSELS [2] which is a non-linear extension of IRLS-MUSSELS. MoDL-MUSSELS (MoDL-M) learns non-linear Fourier domain annihilation relations along with spatial regularization. It is a phase blind recovery scheme with a pre-calibrated approach that uses coil sensitivity information estimated from additional calibration scans on top of main scan. On the other hand, our proposed method does a double (phase and coil sensitivity) blind recovery

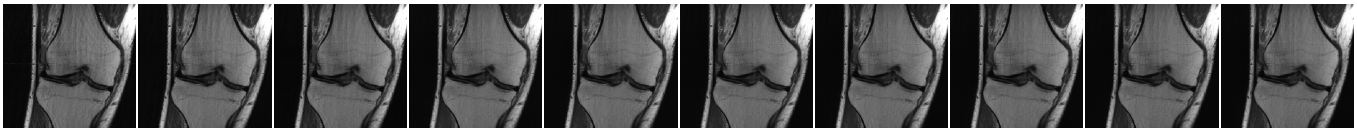

(a) 1st, 26.75 (b) 2nd, 27.78 (c) 3rd, 28.54 (d) 4th, 29.06 (e) 5th, 29.15 (f) 6th, 29.27 (g) 7th, 29.43 (h) 8th, 29.69 (i) 9th, 30.01 (j) 10th, 30.27

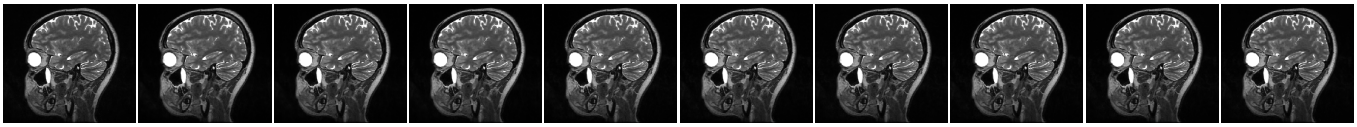

(k) 1st, 21.17 (l) 2nd, 22.39 (m) 3rd, 22.93 (n) 4th, 23.28 (o) 5th, 23.73 (p) 6th, 23.89 (q) 7th, 24.01 (r) 8th, 24.09 (s) 9th, 24.13 (t) 10th, 24.24

Fig. S7. Proposed H-DSLR reconstructions of 4x under-sampled 15-channel knee and 6x under-sampled 12-channel brain data as a function of iterations K from left to right. The images get more de-aliased with increase in iterations. The reported numbers are SNR in dB which improves with iterations.

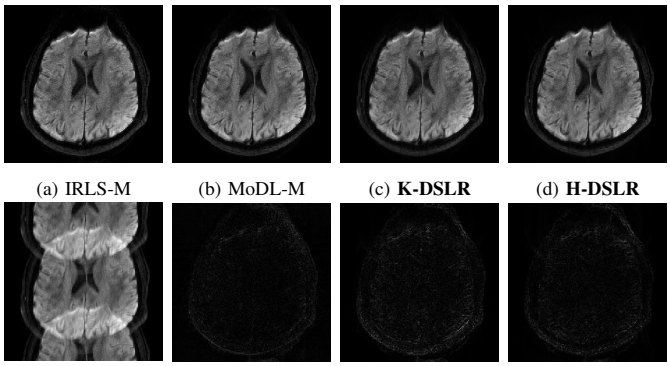

(a) IRLS-M (b) MoDL-M (c) **K-DSLR** (d) **H-DSLR**

(e) $\mathcal{A}^H\mathbf{B}$ (f) MoDL-M (g) **K-DSLR** (h) **H-DSLR**

Fig. S8. 2-shot reconstruction results of 4-channel partial Fourier brain diffusion MRI. IRLS-M (IRLS-MUSSELS) reconstruction was ground truth for training. The proposed schemes are compared against MoDL-M(MoDL-MUSSELS). The top row shows sum-of-squares images from different schemes while the bottom row shows error maps generated from IRLS-M as ground truth. Both K-DSLR and H-DSLR provide performance comparable to MoDL-M.

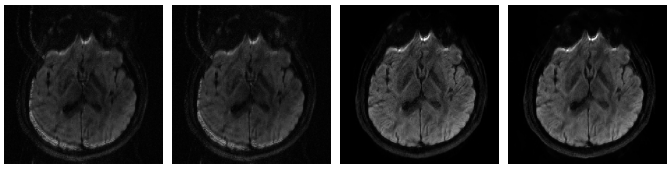

(a) IRLS-M (b) MoDL-M (c) **K-DSLR** (d) **H-DSLR**

Fig. S9. Comparison of calibrated approaches (MoDL-M (MoDL-MUSSELS) and IRLS-M (IRLS-MUSSELS)) with the proposed calibration-less approaches during mismatch in scans. A 2-shot recovery of the 4-channel partial Fourier brain data is shown for comparisons. The acquired k-space measurements were translated in spatial domain to emulate motion. Both calibrated approaches MoDL-M and IRLS-M reconstructions show diagonally striped motion artifacts due to mismatch. Our proposed schemes (K-DSLR and H-DSLR) remain unaffected.

that avoids potential motion artifacts introduced from the sensitivity estimation step. Both the methods were tested on the diffusion data described in Section III-C.

E. Brain Diffusion MRI Recovery

We performed a 2-shot recovery of brain diffusion MRI with the proposed scheme and compared against pre-calibrated MoDL-MUSSELS. All the networks were trained with IRLS-MUSSELS reconstructions as ground truth. The comparisons on one of the slices at a specific direction can be seen in Fig. S8 where error maps are generated by computing absolute differences with IRLS-MUSSELS (ground truth). The H-DSLR and MoDL-MUSSELS reconstructions look sharper at the edges compared to K-DSLR which can be attributed to the spatial prior leveraged by these schemes. K-DSLR error map shows some residual error along the skull region which are further suppressed by the spatial domain prior in H-DSLR. Proposed reconstructions are comparable to MoDL-MUSSELS visually and also through error maps. Note that MoDL-MUSSELS does a phase blind recovery by leveraging coil sensitivity information. On the other hand, the proposed schemes are calibration-less and hence perform a double blind recovery which is more challenging.

F. Benefit over Calibrated Approaches

Pre-calibrated approaches suffer from motion induced artifacts due to mismatch between the calibration and main scans. We demonstrate the benefit of our proposed calibration-less scheme over pre-calibrated MODL-MUSSELS and IRLS-MUSSELS through a simulation experiment. Similar to the parallel MRI case, we introduce a mismatch by modulating the Fourier data with a linearly varying phase term which leads to a shift in spatial domain. The reconstructions results on a test slice is shown in Fig. S9. We observe striped artifacts in both IRLS-MUSSELS and MoDL-MUSSELS reconstructions due to a mismatch between the sensitivities and coil images while our proposed calibration-less approaches remain unaffected. This study shows the benefit of our proposed scheme in avoiding motion artifacts over calibrated approaches.

REFERENCES

[1] M. Mani, M. Jacob, D. Kelley, and V. Magnotta, "Multi-shot sensitivity-encoded diffusion data recovery using structured low-rank matrix completion (MUSSELS)," *Magnetic Resonance in Medicine*, vol. 78, no. 2, pp. 494–507, 2017.

[2] H. K. Aggarwal, M. P. Mani, and M. Jacob, "MoDL-MUSSELS: Model-based deep learning for multishot sensitivity-encoded diffusion mri," *IEEE transactions on medical imaging*, 2019.

[3] M. Mani, H. K. Aggarwal, V. Magnotta, and M. Jacob, "Improved MUSSELS reconstruction for high-resolution multi-shot diffusion weighted imaging," *Magnetic Resonance in Medicine*, 2019.